Review

Direct Z-scheme photocatalytic systems based on vdW heterostructures for water splitting and CO$_2$ reduction: fundamentals and recent advances

Kaiyue Hu[1,#], Jiayu Tian[1,#], Zhifu Zhou[1], Daming Zhao[2], Xiangjiu Guan[1]

[1]International Research Center for Renewable Energy, State Key Laboratory of Multiphase Flow in Power Engineering, Xi'an Jiaotong University, Xi'an 710049, Shaanxi, China.
[2]School of Advanced Energy, Shenzhen Campus of Sun Yat-sen University, Shenzhen 518107, Guangdong, China.
[#]Authors contributed equally.

Correspondence to: Prof. Xiangjiu Guan, International Research Center for Renewable Energy, State Key Laboratory of Multiphase Flow in Power Engineering, Xi'an Jiaotong University, No. 28, Xianning West Road, Xi'an 710049, Shaanxi, China. E-mail: xj-guan@mail.xjtu.edu.cn; Prof. Daming Zhao, School of Advanced Energy, Shenzhen Campus of Sun Yat-sen University, No. 66, Gongchang Road, Shenzhen 518107, Guangdong, China. E-mail: zhaodaming@mail.sysu.edu.cn

Abstract

Photocatalytic water splitting and CO$_2$ reduction are conducive to alleviating the increasingly serious environmental problems and ever-tightening energy problems. Among various modification strategies, constructing Z-scheme heterostructures and direct Z-scheme heterostructures, in particular, by mimicking natural photosynthesis, has been widely researched for the effective separation of photogenerated electrons and holes with strong redox ability. However, a low lattice matching degree of different semiconductors often results in serious crystal defects in the composite. Fortunately, van der Waals (vdW) heterostructures constructed through interlayer weak vdW interactions provide a remedy, which not only can ensure the high quality of Z-scheme heterostructures but also preserve the original properties of individual components and induces new properties at the heterogeneous interfaces. Herein, we introduce the fundamentals of direct Z-scheme vdW heterostructure and review the last five-year progress of direct Z-scheme vdW heterostructures for photocatalytic water splitting and CO$_2$ reduction, highlighting the characteristics and fundamental modification principles of different heterostructures, aiming to provide informative principles for the design of advanced heterostructure photocatalysts for solar energy conversion.

Keywords: Water splitting, CO$_2$ reduction, photocatalysis, direct Z-scheme heterostructure, van der Waals heterostructure

INTRODUCTION

Due to the rapid development of modern industrial civilization, the consumption of fossil energy is increasing day by day. According to the 2023 edition of Statistical Review of World Energy[1], traditional fossil fuels still account for a large proportion of primary energy consumption, comprising 82%, and the non-renewability of fossil fuels leads to the aggravation of the energy crisis. Compared with the previous year, CO_2 emissions from energy utilization and industrial processes increased by 0.8%, indicating that the imbalance of the carbon cycle is further aggravated and environmental problems are deteriorating. In recent years, in order to cope with the energy crisis and solve environmental problems, the development and utilization of renewable energy, such as solar energy and wind energy, came into being. Among them, solar energy has been widely studied because of its advantages of sustainability, pollution-free nature, and richness, but its utilization is limited by time and space dimensions[2]. Since the pioneering discovery of photocatalytic water splitting over TiO_2 by Fujishima and Honda in 1972[3], many developments on advanced photocatalytic systems have been continuously reported. Due to the advantages of H_2, including high energy storage density, high calorific value, non-pollution, and sustainability[4,5], and the fact that the reduction products of CO_2 can be used as high value-added chemicals and fuels[6-8], the research on photocatalytic water splitting into H_2 and CO_2 reduction has become a hot spot in the energy field. Converting solar energy into chemical energy and storing it via photocatalysis in a zero-carbon way can not only solve the intermittent problem of renewable energy but also reduce carbon emissions and the excessive reliance on traditional fossil energy, which is of great significance for solving environmental pollution problems, accelerating the realization of green and low-carbon circular economic development system and carbon peaking and carbon neutrality goals.

As shown in Figure 1, the energy band of a semiconductor photocatalyst is divided into conduction band (CB) and valence band (VB), and the difference between CB minimum (CBM) and VB maximum (VBM) is energy band gap (E_g). Under the irradiation of sunlight, photons with energy greater than the E_g of a semiconductor are absorbed, and the electrons located in the VB of the semiconductor can be stimulated to the CB to become photogenerated electrons (e^-); meanwhile, the corresponding positions in the VB generate photogenerated holes (h^+). Then, the photogenerated electrons and holes migrate to the surface of the photocatalyst, participating in reduction and oxidation reactions, respectively. During the migration process of photogenerated carriers from the bulk to the surface of the photocatalyst, bulk and surface recombination of carriers occurs, accompanied by the release of absorbed energy in the form of light, which is detrimental to the photocatalytic efficiency. For photocatalytic water splitting, the reduction reaction reduces protons to H_2, and the oxidation reaction oxidizes OH^- to O_2; for CO_2 reduction reaction (CO_2RR), the reduction reaction reduces CO_2 to substances such as CO, CH_4 and other hydrocarbons, and the oxidation reaction still oxidizes OH^- to O_2.

To date, numerous modification strategies have been reported to improve the photocatalytic performance, such as solid solution construction[9], nanomaterials development[10,11], morphology control[12,13], heteroatoms doping[14], defect engineering[15], loading cocatalysts[16,17], constructing heterostructures[18,19], *etc*. Among these strategies, mimicking natural photosynthesis by coupling two dissimilar semiconductors to construct a Z-scheme heterostructure is of greater prominence. The Z-scheme heterostructures not only facilitate the separation and migration of photogenerated carriers but also retain strong oxidation and reduction driving forces for photocatalytic reactions. In particular, a direct Z-scheme photocatalytic system does not require an additional electron transfer mediator, reduces the migration distance of photogenerated carriers, avoids the inverse reaction and light shielding effect of an ionic redox mediator, lowers the cost without precious
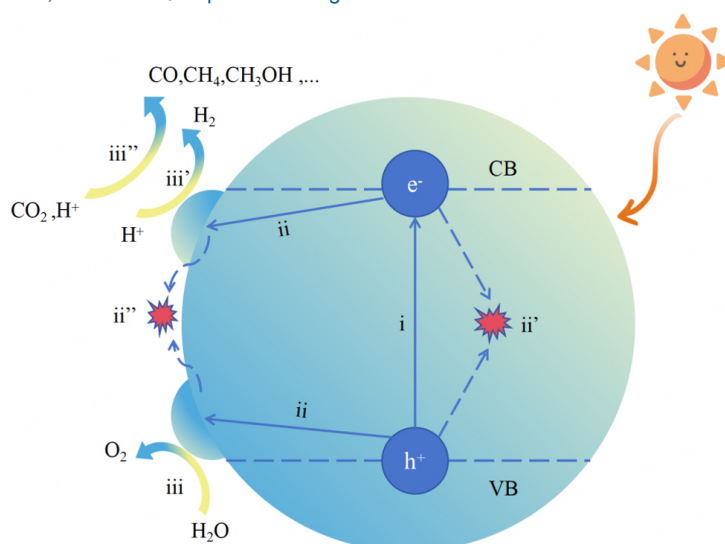
Figure 1. Principles of photocatalytic water splitting reaction & CO_2RR (i) the process of photo-excitation to generate photogenerated electrons and holes, (ii) separation and migration of photogenerated charges; (ii') bulk recombination of photogenerated charges; (ii'') surface recombination of photogenerated charges; (iii) O_2 evolution reaction (OER); (iii') H_2 evolution reaction (HER); (iii'') CO_2RR.

metals, and thus has been widely explored in recent years[20]. It is worth mentioning that direct Z-scheme heterostructures based on van der Waals (vdW) forces between the layers of two-dimensional (2D) materials have attracted widespread interest. The 2D materials are easy to stack together due to the absence of hanging bonds on their surfaces, which gives full play to the advantages of direct Z-scheme heterostructures. At the same time, 2D materials have high specific surface area and good carrier transfer, which are crucial in photocatalytic water splitting and CO_2RR. Although some review articles on papers specifically on Z-scheme heterostructures, photocatalytic water splitting, or CO_2RR have successively appeared[21,22], there has been little comprehensive summarization covering the above topics. This article introduces the research advances of direct Z-scheme vdW heterostructures for photocatalytic water splitting and CO_2RR in the last five years, which is expected to be beneficial and instructive for the design and construction of high-efficiency heterostructure photocatalysts.

FUNDAMENTALS OF DIRECT Z-SCHEME VdW HETEROSTRUCTURE
Z-scheme heterostructures
Inspired by the natural photosynthesis, the Z-scheme artificial photocatalytic system was proposed, which is named after the charge transfer path of letter "Z" type between the two semiconductors. So far, the Z-scheme photocatalytic systems have experienced the 1st generation liquid-mediator Z-scheme photocatalytic system with reversible redox pairs (e.g., Fe^{3+}/Fe^{2+}, IO_3^-/I^-) as the electron transfer chain between the coupled photocatalysts, the 2nd generation solid-mediator Z-scheme photocatalytic system with metal nanoparticles, conductive carbon materials as the electron mediators, and the 3rd generation mediator-free Z-scheme photocatalytic system [Figure 2]. The 1st generation liquid-mediator Z-scheme photocatalytic system was initially proposed by Bard[23], which consists of two semiconductors and reversible redox pairs. The photogenerated electrons located on photocatalyst II (PC II) have stronger reduction capacity, which reduce the electron acceptors to electron donors, and the photogenerated holes located on photocatalyst I (PC I) have stronger oxidation capacity, which oxidize the resulting electron donors, thus realizing the recombination of photogenerated carriers with lower redox capacity through reversible redox pairs. Consequently, a strong redox potential is retained, and then the photocatalytic activity is improved to some extent. However, it is only applicable to a liquid-phase system, which is greatly affected by the pH value of the reaction system, and the decrease of the light absorption capacity of the photocatalyst caused by the presence of redox pairs and the depletion of carriers with higher redox capacity
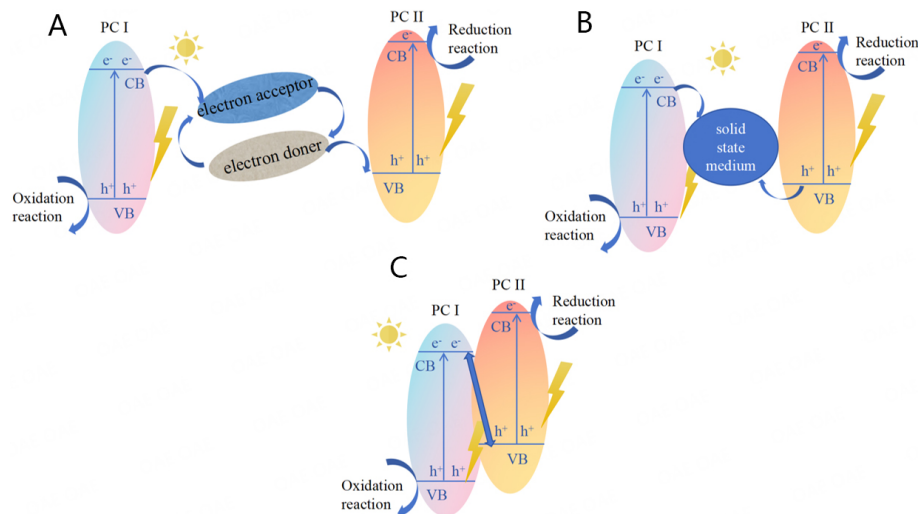
Figure 2. Evolution of Z-scheme heterostructures. (A) The 1st generation liquid-mediator Z-scheme heterostructures; (B) the 2nd generation solid-mediator Z-scheme heterostructures; and (C) the 3rd generation mediator-free Z-scheme heterostructures.

(reverse reaction) should not be neglected. Thus, the liquid-mediator Z-scheme photocatalytic system has gradually faded out of vision.

Compared with the liquid-mediator Z-scheme photocatalytic system, the 2nd generation solid-mediator Z-scheme photocatalytic system, consisting of two different semiconductors and solid-state electron mediators, expands the application range to gas phase, liquid phase and solid phase, which can effectively inhibit redox pairs from reacting with the carriers with strong redox ability. Nevertheless, the strong optical absorption of solid-state electron mediators reduces the utilization of light energy over semiconductor photocatalysts, and the usage of noble metals will increase the cost, which limits its practical application.

To address the problems of liquid-mediator Z-scheme heterostructures and solid-mediator Z-scheme heterostructures, Wang *et al*. proposed a 3rd generation mediator-free Z-scheme system based on ZnO and CdS[24], which was subsequently named the direct Z-scheme system by Xu *et al*. in 2013[25] and is currently commonly used in the field of photocatalysis. In a direct Z-scheme system, photogenerated electrons located in the lower CB position and photogenerated holes located in the higher VB position of the composites can directly recombine without an additional electron transfer mediator. As a result, the strong redox capability is retained, accompanied by discarded reverse reaction, light shielding effect and reduced system cost, which make the direct Z-scheme system attract constant and extensive research, including the S-scheme heterostructure proposed by Fu *et al*. in 2019, which is also an interpretation of the mechanism of the 3rd generation mediator-free Z-scheme heterostructure[26]. For example, Chen *et al*. successfully prepared a C,N co-doped TiO_2/g-C_3N_4 direct Z-scheme heterostructure and found that the H_2 production rate of 3 wt% C,N-TiO_2 NPs/g-C_3N_4 was increased by 20.3-fold compared to that of pure g-C_3N_4, with a significant improvement in light absorption properties[27]. Low *et al*. synthesized a TiO_2/CdS direct Z-scheme heterostructure and showed that the accelerated photogenerated charge separation in the direct Z-scheme system led to a significant improvement in the performance for CO_2RR compared to each individual component, by folds of up to 6.3 times and 5.2 times in comparison to TiO_2 and CdS, respectively[28].

vdW Heterostructures

The fabrication of conventional heterostructures with interfacial chemical bonds often requires considering the lattice matching degree of different semiconductors to minimize crystal defects in the composite,

whereas lattice matching is less restrictive for vdW heterostructures formed through weak vdW forces between the coupled semiconductors. In 1984, Koma *et al.* successfully synthesized a high-quality heterostructure of sub-nanometer thickness by vdW epitaxy for the first time[29], which relies on weak vdW interactions to release the stresses stemming from the lattice mismatch, thus minimizing crystal defects. In the case of vdW heterostructures, the weak vdW forces formed between the layers of semiconductor materials, as opposed to strong chemical bonds, offer the flexibility of stacking layers with different lattice constants and orientations without significant strain, leading to novel crystal phases and properties (e.g., tunable chemical and physical properties, adjustable energy band structure with different stacking sequences, *etc.*); the photogenerated carriers are produced in atomically thin layers[30], shortening the carrier migration distance from the body to the surface of the photocatalyst, ensuring maximal participation of photogenerated carriers in surface reactions. When different semiconductors come into contact, the difference in their Fermi levels causes electrons to spontaneously flow from the semiconductor with a higher Fermi level to that with a lower Fermi level. This results in the accumulation of electrons at the interface of the semiconductor with a lower Fermi level, thereby creating a built-in electric field directed from the high Fermi level semiconductor to the low Fermi level semiconductor. The photogenerated electrons at the CB and photogenerated holes at the VB of both semiconductors migrate under the driving of this built-in electric field. Figure 3 provides a simple schematic of a Z-scheme heterostructure based on vdW forces, where photogenerated carriers transfer follows a Z-scheme pathway driven by the built-in electric field, resulting in the accumulation of electrons and holes in the more negative CB and more positive VB, respectively. Therefore, it is beneficial to construct direct Z-scheme heterostructures based on vdW forces to break the limitation of lattice mismatch of different materials and to further accelerate the interlayer charge transfer. For example, Xu *et al.* constructed $Bi_3O_4Cl/g-C_3N_4$ vdW heterostructures for CO_2RR in ethanol and found that the vdW forces between layers can effectively promote the transfer of photogenerated electrons from $g-C_3N_4$ to Bi_3O_4Cl and strengthen the separation of photogenerated carriers, greatly improving the photocatalytic performance[31]. Additionally, compared to the heterostructure with interfacial chemical bonds, the direct interface interaction in a vdW heterostructure is relatively weak, but it owns a simpler structure and greater adjustability, thus allowing for a wider range of component semiconductors and cheaper preparation costs.

## APPLICATIONS OF DIRECT Z-SCHEME vdW HETEROSTRUCTURES

Photocatalytic water splitting

Graphitic carbon nitride-based materials

Since the discovery of graphene with its unique hexagonal structure, the applications of graphene-like materials have been constantly developed. Additionally, 2D graphitic carbon nitride (CN) materials, such as $g-C_3N_4$[32] and $g-C_6N_6$[33], are increasingly gaining ground due to their high stability, low cost, and non-toxicity. However, most CN materials find it challenging to split pure water alone, limited by the thermodynamic contradiction between optical absorption and redox potentials and a high recombination rate of photogenerated carriers. To solve the problem mentioned above, some CN materials-based 2D/2D direct Z-scheme vdW heterostructures have recently been developed for photocatalytic water splitting. For instance, Zhang *et al.* reported a $PtS_2/g-C_3N_4$ vdW heterostructure for photocatalytic water splitting through first principles calculation[34]. Calculation results show that this heterostructure is a direct Z-scheme heterostructure with an indirect interlayer band gap of 1.98 eV [Figure 4A and B]. The heterostructure has a high light absorption rate of 5.82×10^5 cm^{-1} at 400 nm, which could induce photocatalytic water splitting when pH = 0. When the biaxial strain changes in the range of -6% to 6%, especially when tensile strain is applied, the absorption of visible light by the composite photocatalytic system is significantly redshifted [Figure 4C], which is beneficial for the utilization of visible light. More strikingly, the theoretical solar-to-H_2 (STH) efficiency of a $PtS_2/g-C_3N_4$ heterostructure reaches 31.64% [Figure 4D], making it a promising heterostructure for photocatalytic water splitting. Yang *et al.* reported a $g-C_6N_6/WTe_2$ vdW heterostructure
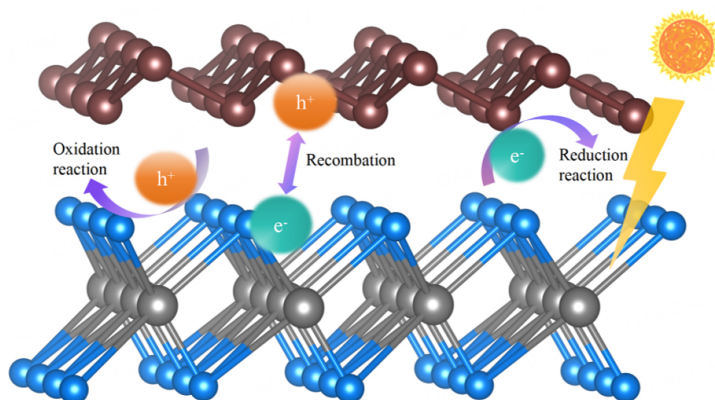
**Figure 3.** Schematic diagram of Z-scheme heterostructure based on vdW forces.
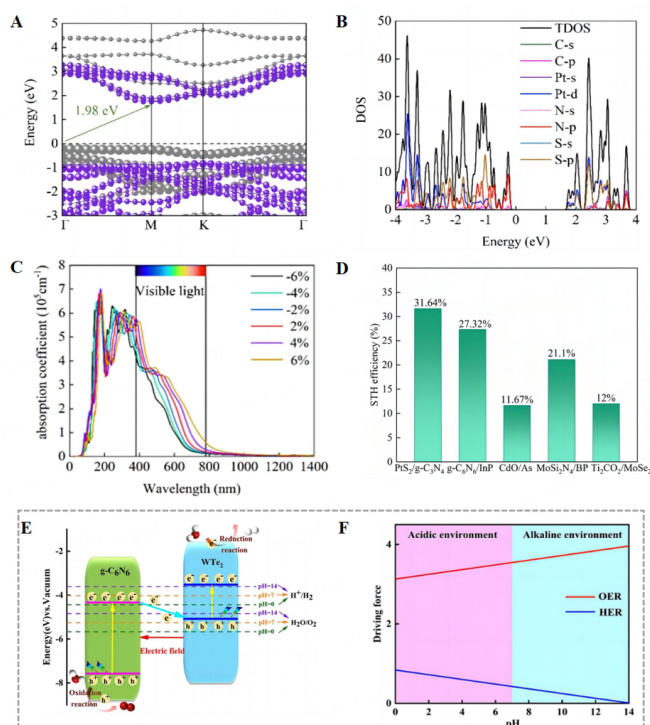
Figure 4. (A) Band structures of the PtS_2/g-C_3N_4 vdW heterostructure. (Reproduced with permission[34]. Copyright 2023, Elsevier); (B) Projected density of states (DOS) of the PtS_2/g-C_3N_4 vdW heterostructure. (Reproduced with permission[34]. Copyright 2023, Elsevier); (C) Absorption spectrums of the PtS_2/g-C_3N_4 vdW heterostructure under various biaxial strains. (Reproduced with permission[34]. Copyright 2023, Elsevier); (D) The STH efficiency of other 2D materials compared with PtS_2/g-C_3N_4 vdW heterostructure. In plot (A), the purple and gray lines indicate the contributions from the monolayers PtS_2 and g-C_3N_4, respectively, and the horizontal black dashed line set to zero energy represents the Fermi level. (Reproduced with permission[34]. Copyright 2023, Elsevier); (E) The direct Z-scheme photocatalytic mechanism for water splitting in the g-C_6N_6/WTe_2 heterostructure. (Reproduced with permission[35]. Copyright 2022, Elsevier); (F) The variation of driving forces for OER and HER with pH value. (Reproduced with permission[35]. Copyright 2022, Elsevier).

based on single-layer WTe_2 with excellent photoelectric properties [Figure 4E] and used the formation energy E_f to evaluate the stability of the heterostructure[35]. E_f can be obtained from Equation $E_f = E_{g\text{-}C6N6/WTe2}$ - E_{WTe2}-$E_{g\text{-}C6N6}$, in which $E_{g\text{-}C6N6/WTe2}$, and $E_{g\text{-}C6N6}$ denote the total energies of the g-C_6N_6/WTe_2 heterostructure, isolated WTe_2 and g-C_6N_6 monolayers, respectively. The smaller the E_f value, the more stable the heterostructure is. Calculation results show that the g-C_6N_6/WTe_2 heterostructure is a direct Z-scheme heterostructure in which the reduction reaction and oxidation reaction respectively occur on WTe_2 and g-C_6N_6, thus effectively inhibiting the recombination of photogenerated carriers. Furthermore, the CB of WTe_2 and the VB of g-C_6N_6 can cover the reduction/oxidation potentials of pure water splitting. Finally, the CB of WTe_2 and the VB of g-C_6N_6 can cover the reduction/oxidation potentials of pure water splitting.

Finally, the theoretical STH efficiency reaches 57%~59%, which effectively improves the visible-light utilization of single g-C_6N_6 limited by its wide band gap. In addition, the influence of pH on photocatalytic water splitting was also discussed [Figure 4F], and results showed that an appropriate pH for both O_2 evolution reaction (OER) and H_2 evolution reaction (HER) is crucial for pure water splitting.

Several studies have discussed the effects of interlayer interactions and intralayer electric fields on photocatalytic performance of direct Z-scheme vdW heterostructures, which are essential for guiding the optimization of heterostructure photocatalysts. For example, Zhang *et al.* constructed a 2D C-doped boron nitride (BCN)/C_2N direct Z-scheme vdW heterostructure[36]. From the transient plots of excited electrons and holes [Figure 5A and B], the authors estimated that electron-hole recombination in the heterostructure occurs within 2 ps, including up to 85% through interlayer transfer between BCN and C_2N. This suggests that most recombination of photogenerated carriers occurs between BCN and C_2N layers, effectively weakening the recombination within BCN and C_2N themselves. It was proposed that if the interlayer band gap of a 2D vdW heterostructure was smaller than that of each individual component, i.e., the intralayer band gap, then ultrafast interlayer electron-hole recombination can be realized in vdW heterostructures due to the intralayer optical phonon modes and interlayer shear phonon mode induced by vdW interaction so that holes and electrons with relatively stronger redox ability can be retained, which is of enlightenment significance for constructing direct Z-scheme vdW heterostructures[36]. Wang *et al.* constructed a direct Z-scheme heterostructure based on C_7N_6 and Janus GaSnPS monolayers and revealed the important role of the built-in electric field of Janus GaSnPS monolayer for accelerating photogenerated carrier separation[37]. Due to the lack of inversion symmetry in the Janus GaSnPS monolayer, the effects of its P and S surfaces are not equivalent. Then, two modes of vdW heterostructure are constructed, i.e., C_7N_6/PSn-GaS and C_7N_6/SGa-SnP. The 2D plane-integrated electron density difference and electrostatic potentials demonstrate that the different built-in electric field directions of Janus GaSnPS monolayers in varied modes of heterostructures lead to diverse effective electric fields of the heterostructure [Figure 5C-F], thus resulting in distinct band gaps of the two modes. This presents a comprehensive strategy for modulating the band gap of heterostructures, enabling their application in overall water splitting under visible light, independent of sacrificial agents. This approach paves the way for more efficient and sustainable water splitting processes. Besides, based on BC_3/C_3N and BC_3/BC_6N direct Z-scheme vdW heterostructures, Wang *et al.* focused on the effects of π-π interaction on the stacking configuration, interlayer coupling, electronic structure, and photocatalytic performance of heterostructures[38] and found that the interaction between heterostructure layers is composed of the electrostatic π-π repulsion interaction between benzene rings and the electrostatic attraction interaction between B and N atoms of different constituent layers in the heterolayer, and the two heterostructures both play a role in improving the light absorption performance of BC_3, among which BC_3/C_3N has an absorption spectrum of visible and even near-infrared light. This study is of great significance for constructing heterostructures of similar materials.

In addition to interlayer interactions and intralayer electric fields, heteroatoms doping plays a synergistic role in improving the photocatalytic properties of direct Z-scheme vdW heterostructures. For example, Dong *et al.* constructed a Z-scheme heterostructure by combining CN with a small amount of BCN[39] and verified the successful formation of vdW heterostructure by comprehensive analysis of X-ray diffraction, X-ray photoelectron spectroscopy, transmission electron microscopy [TEM, Figure 6A], and atomic force microscopy. The direct Z-scheme vdW heterostructure greatly improved the separation efficiency of photogenerated electrons and holes, contributing to a higher H_2 production rate and apparent quantum efficiency (AQE), reaching 3,357.1 μmol h^{-1} g^{-1} and 16.3 % at 420 nm, respectively [Figure 6B and C]. Besides, the optimal CN/BCN-0.5% sample remained stable after 15 H_2-production cycles, showing excellent photocatalytic performances. Likewise, Meng *et al.* proposed a C_7N_6/Sc_2CCl_2 heterostructure[40] and
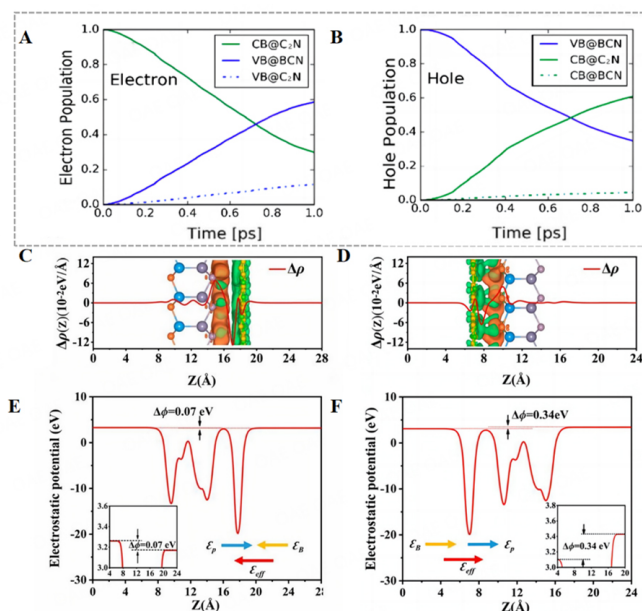
Figure 5. (A) The time-dependent electron and (B) hole population of BCN/C_2N heterostructure. (Reproduced with permission[36]. Copyright 2018, American Chemical Society); (C and D) 2D plane-integrated electron density difference along the Z direction for the C_7N_6/PSn-GaS and C_7N_6/SGa-SnP heterostructures. 3D isosurfaces of the electron density difference of the two heterostructures are plotted in the insets of this figure. The isosurface level is 0.0001e Å^{-3}. The orange and green regions represent electron accumulation and depletion, respectively. (Reproduced with permission[37]. Copyright 2023, American Chemical Society); (E and F) Electrostatic potentials of C_7N_6/PSn-GaS and C_7N_6/SGa-SnP heterostructures. The horizontal arrows indicate the directions of the electric fields. The blue, yellow, and red arrows stand for the Janus layer, interfacial, and total effective electric fields, respectively. (Reproduced with permission[37]. Copyright 2023, American Chemical Society).
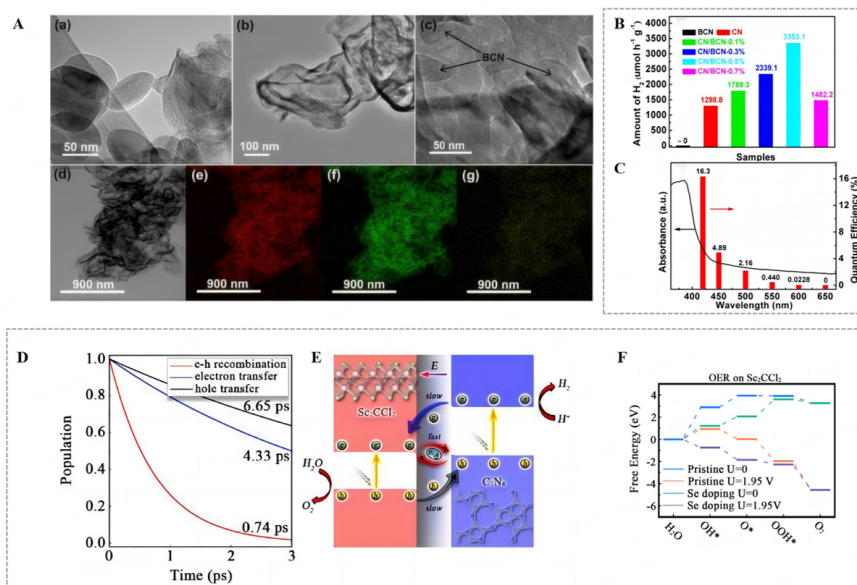
Figure 6. (A) TEM images of (a) BCN, (b) CN and (c) CN/BCN-0.5% samples; (d-g)TEM EDX elemental mappings of CN/BCN-0.5% sample. (Reproduced with permission[39]. Copyright 2020, Elsevier); (B) H_2 production rate of different samples of CN/BCN heterostructures under the visible light (λ > 420 nm). (Reproduced with permission[39]. Copyright 2020, Elsevier); (C) Wavelength-dependent AQE of CN/BCN-0.5% sample. (Reproduced with permission[39]. Copyright 2020, Elsevier); (D) The electron-hole recombination and electron and hole transfer dynamics in C_7N_6/Sc_2CCl_2 heterostructures, where the time constants are fitted by the exponential function corresponding to three processes. (Reproduced with permission[40]. Copyright 2022, American Chemical Society); (E) Charge transfer in C_7N_6/Sc_2CCl_2 heterostructure. (Reproduced with permission[40]. Copyright 2022, American Chemical Society); (F) Processes occurring on the C_7N_6/Sc_2CCl_2 surface at pH 7. The blue and orange short lines stand for intermediate states in HER/OER processes on the undoped heterostructure with or without light-induced bias potential *U*, whereas the green and purple short lines stand for intermediate states in the OER processes occurring on the doped S atom. (Reproduced with permission[40]. Copyright 2022, American Chemical Society).

proved that this heterostructure has a broad spectral absorption extending from the ultraviolet (UV) region to the near-infrared region due to its narrow band gap of 0.17 eV between the CBM of Sc_2CCl_2 and the VBM of C_7N_6, which mainly depends on the interlayer transition near Γ point in momentum space. The time constant calculation shows the faster interlayer carrier recombination in the heterostructure compared to the electrons transfer between two CB or holes transfer between two VB [Figure 6D and E], confirming that the Z-scheme heterostructure contributes to the retention of a strong redox capacity. Consequently, the photocatalytic water reduction over C_7N_6/Sc_2CCl_2 can occur spontaneously, and the photocatalytic water oxidation can also happen spontaneously with Se doping in the surface of Sc_2CCl_2 [Figure 6F].

Transition-metal dichalcogenides-based materials
Transition-metal dichalcogenides (TMDs) MX_2 (M is a transition metal atom, and X is a sulfur atom) have been extensively studied in the photocatalysis field due to the graphene-like structure with excellent optoelectronic properties and mechanical properties[41-43]. Most TMDs can be used for visible-light photocatalytic H_2 production due to their suitable band gaps and energy band positions, but they cannot be used for O_2 production as their VBM cannot cross the oxidation potential of water. Therefore, coupling TMDs with other O_2-evolving photocatalysts to form direct Z-scheme vdW heterostructures is of great importance for expanding the response range of photocatalysts that can facilitate overall water splitting driven by visible light.

Ren *et al.* constructed a PtS_2/arsenene vdW heterostructure and investigated its structural stability, photocatalytic activity, light absorption properties, and STH efficiency based on first-principles calculations[44]. Calculation results show that the heterostructure is a direct Z-scheme system and can achieve an ultrahigh STH efficiency of 49.32%. Zhang *et al.* studied a CdO/HfS_2 vdW heterostructure, and the calculated charge density difference between the interfaces of CdO and HfS_2 indicates that the CdO/HfS_2 heterostructure is a direct Z-scheme heterostructure, and the heterostructure has an excellent visible-light absorption performance, with the absorption peak reaching up to 7.21×10^4 cm^{-1} at 465 nm[45]. Li *et al.* respectively constructed 2D C_3N/WTe_2 and C_3N/WS_2 vdW heterostructures, and the comprehensive analysis on electronic properties, Bader charge and charge density difference distributions reveals that the energy bands of C_3N/WTe_2 are arranged in a Type-I configuration, which is unfavorable for the separation of photogenerated electrons and holes[46]. On the contrary, the C_3N/WS_2 heterostructure is a Z-scheme configuration, which has excellent visible light response, and its band edge position covers the redox potential of water. Strikingly, this study found carbon atoms to be reasonable sites for HER and OER by calculating the Gibbs free energy for H_2 precipitation reactions and the overpotential for O_2 precipitation reactions. Singh *et al.* investigated a series of direct Z-scheme vdW heterostructures by coupling MoS_2, Janus MoSSe with common 2D materials such as TMDs and transition metal oxides (TMOs), and $MoSSe/HfS_2$, $MoSSe/TiS_2$, $MoS_2/T-SnO_2$, and $MoSSe/ZrS_2$ demonstrated excellent photocatalytic properties[47]. Wang *et al.* constructed three direct Z-scheme vdW heterostructures of $MoTe_2/XS_2$ (X = Hf, Sn, Zr) [Figure 7A] and analyzed their structural stability, electronic properties and optical properties[48]. The Bader charge analysis shows that the charge migration in $MoTe_2/SnS_2$ is the largest among the three

heterostructures. Light absorption coefficient calculation (Equation $\alpha(\omega) = \sqrt{2}\omega\sqrt{\sqrt{\varepsilon_1^2(\omega) + \varepsilon_2^2(\omega)} - \varepsilon_1(\omega)}$, where ω represents the angular frequency in vacuum, $\alpha(\omega)$ represents light absorption coefficient, and $\varepsilon_1(\omega)$ and $\varepsilon_2(\omega)$ represent the real part and imaginary part of the dielectric function, respectively.) revealed that the absorption spectra of the heterostructures have a significant redshift compared to $MoTe_2$ or XS_2 monolayers, enabling the optical utilization from visible to near-infrared light spectrum, which is mainly due to the fact that the interlayer band gap of the heterostructure is smaller than an intralayer band gap. The results provide a reference for designing advanced $MoTe_2$-based photocatalysts. Based on the excellent electronic, optical and physical properties of $MoTe_2$ and the superior covalent properties of boron arsenide, Cao *et al.*
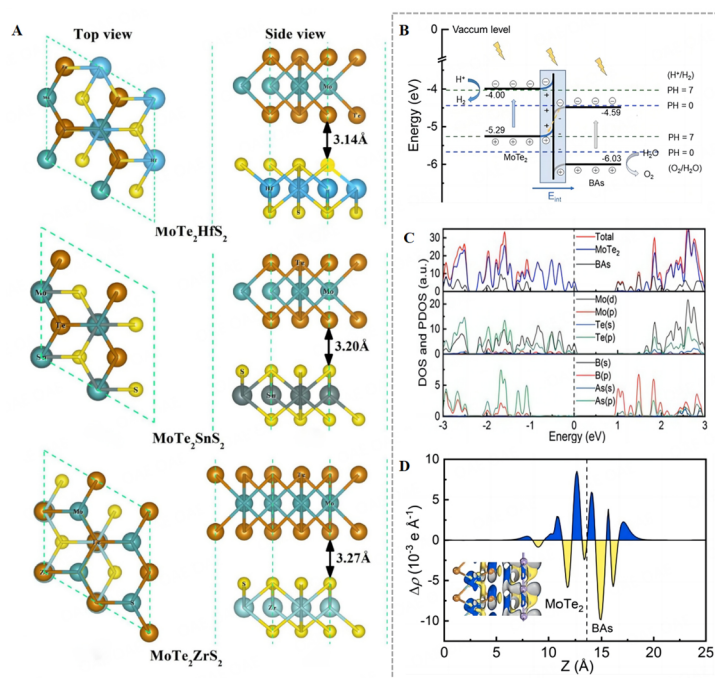
Figure 7. (A) The optimized geometries of $MoTe_2/XS_2$ (X = Hf, Sn, Zr) heterostructures. Claybank, ultramarine, yellow, blue, cyan, and emerald balls represent Te, Mo, S, Hf, Sn, and Zr atoms, respectively, as labeled in the picture above. Left: the top view of the heterostructures; right: the side view of the heterostructures. (Reproduced with permission[48]. Copyright 2020, Elsevier); (B) The schematic diagram of photocatalysis of $MoTe_2/BAs$ heterostructure Z-scheme mechanism. (Reproduced with permission[49]. Copyright 2021, Elsevier); (C) DOS and PDOS of $MoTe_2/BAs$ heterostructure using HSE06 functional. (Reproduced with permission[49]. Copyright 2021, Elsevier); (D) Average charge density difference of the heterostructure along the Z-axis direction. The blue area (positive value) and the yellow area (negative value) represent the accumulation and consumption of electrons, respectively (the inset image shows 3D isosurface of the heterostructure, with the level at 0.0005 e $Å^{-3}$). (Reproduced with permission[49]. Copyright 2021, Elsevier).

carried out a density functional theory study on the 2D heterostructure of $MoTe_2$/boron arsenide[49], and its Z-scheme mechanism, density of states (DOS) and projected DOS (PDOS), and average charge density difference of the heterostructure along the Z-axis direction are shown in Figure 7B-D, respectively. Calculation results indicated that the $MoTe_2$/boron arsenide heterostructure enables photocatalytic water splitting occurring within the pH range of 0~7, with higher light absorption coefficients in the visible light (up to 5.2×10^4 cm^{-1}) compared to that of monolayer components (4.0×10^4 cm^{-1} for $MoTe_2$ monolayer and 3.2×10^4 cm^{-1} for boron arsenide monolayer), higher STH (56.32%) compared to other direct Z-scheme vdW heterostructures (49.32%, 10.5%, and 9.3% for PtS_2/arsenene, $MoSe_2/SnSe_2$, and $WSe_2/SnSe_2$ heterostructures respectively).

Several studies have investigated the effects of built-in electric field, biaxial strain and pH on photocatalytic water splitting reactions. For instance, based on the characteristics of transition metal chalcogenides and arsenene, Zhu *et al.* constructed arsenene/HfS_2 direct Z-scheme vdW heterostructures, whose band edge position satisfies the conditions of overall water splitting[50]. Due to the Fermi level difference between arsenene and HfS_2, the redistribution of charges near the contact interface forms a built-in electric field from arsenene to HfS_2 [Figure 8A], then the photogenerated electrons at the CB of HfS_2 will transfer through the interface to the VB of arsenene and recombine with the photogenerated holes, i.e., a Z-scheme path [Figure 8B], which improves the separation rate of photogenerated carriers with strong redox ability. On this basis, the influence of biaxial strain and pH on the heterostructure is explored. As shown in Figure 8C, it is found that when the biaxial strain changes in the range of -5%~5%, the band gap of arsenene
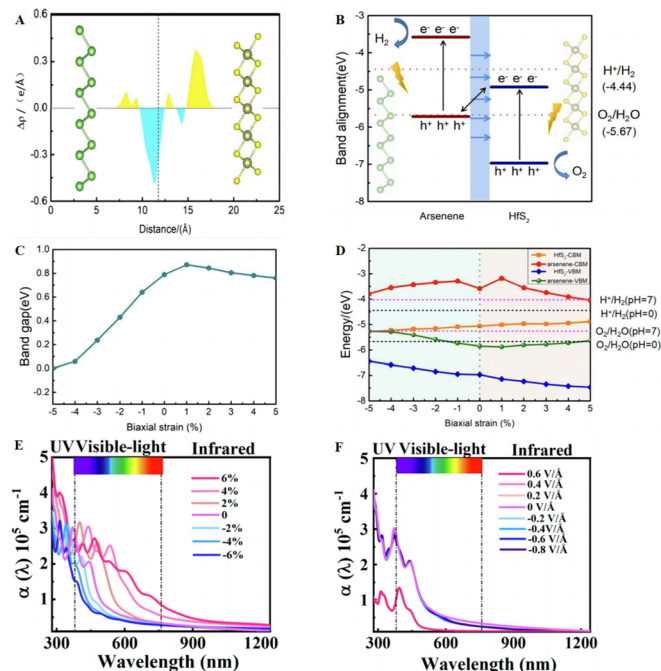
Figure 8. (A) Planar-averaged charge density difference of arsenene/HfS$_2$ heterostructure along the Z direction. The blue and yellow regions represent charge depletion and charge accumulation, respectively. (Reproduced with permission[50]. Copyright 2021, Elsevier); (B) Band edge position of arsenene/HfS$_2$ heterostructure after contact. (Reproduced with permission[50]. Copyright 2021, Elsevier); The band gap (C) and band edge positions (D) of arsenene/HfS$_2$ heterostructure under various biaxial strains from -5 % to 5 % by HSE06. (Reproduced with permission[50]. Copyright 2021, Elsevier). The optical adsorption coefficients of the GaN/BS heterostructures under different (E) biaxial strains and (F) external electric fields (where the value of wavelength ranges from 280 to 1,240 nm). (Reproduced with permission[51]. Copyright 2022, Elsevier).

/HfS$_2$ heterostructure decreases with the increase of compressive strain, but it is not affected by tensile strain. In addition, the heterostructure keeps its photocatalytic activity stable in both neutral (pH = 7) and acidic (pH = 0) environments [Figure 8D]. Similarly, Wang *et al.* built a MoSe$_2$/HfS$_2$ direct Z-scheme vdW heterostructure for overall water splitting[41]. The light absorption range of this heterostructure was significantly widened compared with that of the original monolayer MoSe$_2$ and HfS$_2$, with an obvious absorption peak at a wavelength larger than 400 nm, which mainly benefits from the newly generated interlayer band gap between the CBM of HfS$_2$ and the VBM of MoSe$_2$ in the heterostructure. Additionally, it is verified that the heterostructure manages to maintain its band edge positions in a near-perfect manner under applied strains of -6% to 6%. Relying on first principles, Luo *et al.* investigated the photoelectric properties of GaN/boron sulfide vdW heterostructures and showed that these heterostructures are direct Z-scheme photocatalysts with energy band edges fulfilling the requirements for the overall water splitting[51]. The effects of biaxial strain and external electric field on the photocatalytic performance of GaN/ boron sulfide were investigated, and it was found that compressive strains had a good effect on improving the H$_2$ evolution of the heterostructures [Figure 8E], whereas tensile strains had an unfavorable effect. Strikingly, when a biaxial strain of ε = 6% is employed, the STH efficiency of the GaN/boron sulfide heterostructure is significantly improved to 19.95% compared to that of no strain applied (5.42%). When applying an external electric field in the opposite direction to its inbuilt electric field, the band edge position of the heterostructure shifts upward with the external electric field enhancing, resulting in an enlarged band gap and a blue shift in the absorption spectrum [Figure 8F]. In addition, the heterostructure has a good photocatalytic stability both in neutral and acidic environments. This study is a theoretical guide for the application of biaxial strain and applied electric field for adjusting the band edge positions and band gaps of

heterostructures. Liu *et al*. designed a direct Z-scheme vdW heterostructure consisting of β-GeSe and HfS_2 exhibiting a strong light absorption from UV to visible light and found that the heterostructure can spontaneously carry out photocatalytic water splitting reactions with pH varying from 7 to 12, and its STH efficiency can reach 37.95%[52].

The role of energy band bending in direct Z-scheme vdW heterostructures has also been studied. Cao *et al*. constructed a 2D $WSeTe/XS_2$ (X = Hf, Sn, Zr) vdW heterostructure[53] and indicated that the heterostructure accelerates the separation of photogenerated carriers due to the energy band bending and built-in electric field induced by the Fermi level equilibrating between WSeTe and XS_2 [Figure 9A]. In addition, the absorption spectrum of the heterostructure covers the entire visible light range, significantly improving the light absorption performance of a single XS_2 material. Zhang *et al*. constructed a GeC/HfS_2 direct Z-scheme vdW heterostructure, in which the CBM of GeC is higher than the water oxidation potential and the VBM of HfS_2 is lower than the water reduction potential, boasting carrier mobilities up to 5,823 cm^2 V^{-1} s^{-1}[54]. A work function difference of 0.4 eV between GeC and HfS_2 exists in this heterostructure [Figure 9B], and resultant interfacial energy band bending leads to an accelerated interlayer charge transfer along a Z-scheme path [Figure 9C].

In addition, a number of other approaches have been used to enhance the photocatalytic performance of TMDs, including passivation by Al_2O_3 to reduce surface defects and thus inhibit carrier recombination, introducing MXenes (a tunable family of 2D Carbides and Nitrides[55]) with strong antioxidant capacity to inhibit the photocorrosion of TMDs, using the interactions of intrinsic dipole of the polar material with the built-in electric field of the heterostructure to enhance carriers separation, introducing defects or doping, *etc*. For example, Lu *et al*. successfully developed a direct Z-scheme vdW heterostructure of $SnSe_2/SnSe$ by a two-step vapor phase deposition method [Figure 10A][56] and indicated that the heterostructure has better photocatalytic performance than the original monolayer $SnSe_2$ and SnSe. The stability of the $SnSe_2/SnSe$ heterostructure can be further improved by Al_2O_3 passivation, mainly because Al_2O_3, as a dense oxide film, can play a role in reducing the surface defects of the heterostructure, thereby inhibiting the carrier recombination with the defect as the recombination center, which is of great significance for improving the stability of photocatalysts. Fu *et al*. proposed a direct Z-scheme vdW heterostructure by combining $TiCO_2$ (MXenes) with $MoSe_2$ to solve the limitations of high carrier recombination rate and photocorrosion originating from the oxidation of sulfur group elements by photogenerated holes in monolayer $MoSe_2$ [Figure 10B][57]. Figure 10C and D demonstrate that about 60% of the electrons and 65% of the holes transfer through the interlayer within 0.5 ps, which greatly inhibits the intralayer recombination. Finally, this $TiCO_2/MoSe_2$ heterostructure can achieve a theoretical STH efficiency of 12%. Liu *et al*. investigated the effect of intrinsic dipoles on the charge transfer at heterostructure interfaces by an In_2Se_3/SnP_3 direct Z-scheme heterostructure[58]. When the built-in electric field induced by charge transfer is in the same direction as that of the intrinsic dipole of the In_2Se_3 polarization layer, the photogenerated charge separation is significantly improved, and the STH efficiency of this heterostructure reaches 19.26 %, which provides a reference for the development of high-efficiency photocatalysts based on polar materials. Ju *et al*. systematically investigated the effect of polarization on photocatalysis and found that polarization plays an important role in regulating the adsorption behavior and carrier separation[59]. Improved photocatalytic performance is attributed to differences in surface electrostatic energy, which leads to the accumulation of positive and negative radicals on different surfaces, making it possible to tune the performance of the photocatalysts by controlling the direction and magnitude of the polarization. Jalil *et al*. investigated H and H-phase of $MoSi_2N_4/MoSX$ (X = S, Se) vdW heterostructures, where the H-phase of $MoSi_2N_4/MoSX$ heterostructure has a hexagonal crystal structure exhibiting hexagonal symmetry, and the H-phase of $MoSi_2N_4/MoSX$ heterostructure has a twisted octahedral structure exhibiting trigonal symmetry[60]. For
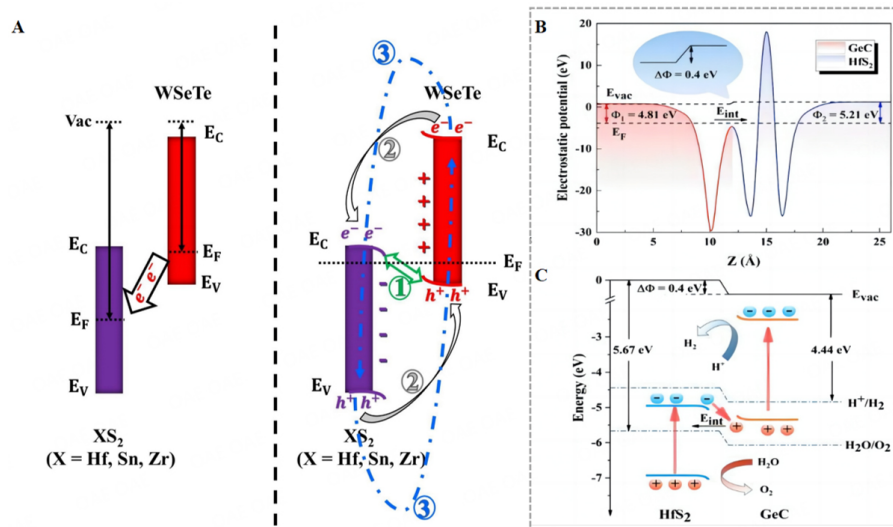
Figure 9. (A) The schematic illustration of the charge transfer paths of direct Z-scheme $WSeTe/XS_2$ (X = Hf, Sn, Zr) heterostructures: (left) before contact, (right) after contact. (Reproduced with permission[53]. Copyright 2022, Elsevier); (B) The electrostatic potential diagrams of the GeC/HfS_2 heterostructure. (Reproduced with permission[54]. Copyright 2023, AIP Publishing); (C) Band arrangement and Z-scheme photocatalytic mechanism of the GeC/HfS_2 heterostructure. (Reproduced with permission[54]. Copyright 2023, AIP Publishing).

HER, the ideal H adsorption capacity of photocatalysts should not be too strong or too weak to ensure the H adsorption and desorption of products. Compared with the strong H adsorption capacity of N defects and the weak H adsorption capacity of Si defects, S/Se defects show a moderate-intensity interaction with H, which is favorable for HER. Shahrokhi *et al.* demonstrated, based on density functional theory calculations, that the electronic properties and photocatalytic performance of 2D $\alpha\text{-}MoO_{3-x}S_x/2H\text{-}MoS_{2-x}O_x$ heterostructure can be modulated via heterovalent anion doping ($\alpha\text{-}MoO_{3-x}S_x$ and $2H\text{-}MoS_{2-x}O_x$)[61]. It is found that the heterostructure type of $MoO_{3-x}S_x/MoS_2$ heterostructures varies with the doping of S elements in MoO_3 [Figure 10E]. At low S doping concentration (≤ 5%), the heterostructure presents as type III, but when S doping concentration is 9%~10%, the heterostructure was found to be a direct Z-scheme photocatalyst. Figure 10F shows the increasing interlayer band gap and decreasing Bader charge transfer with increasing S concentration.

Arsenene-based materials
Arsenene, possessing a graphene-like structure, has attracted much attention for its outstanding advantages such as high carrier mobility, anisotropy of heat transfer, and an indirect band gap of ~2.2 eV[62-64]. In recent years, some arsenene-based direct Z-scheme vdW heterostructures have been reported.

Lu *et al.* constructed a heterostructure of $InSe_2/arsenene$[65], and different configurations were proposed using supercell matching (2 × 2 × 1 arsenene supercells and 3 × 3 × 1 $\alpha\text{-}In_2Se_3$ supercells) [Figure 11]. The high structure stability shown in Figure 11A and F at room temperature was demonstrated by calculating the electron binding energy (E_b) and AIMD simulations. Thanks to the high interlayer potential drop, the formed built-in electric field can effectively accelerate the separation of photogenerated carriers in the heterostructure. Finally, the two heterostructures achieve a high STH efficiency of 57.08 % and 24.67 %, respectively, which are higher than that of $InSe_2$ and arsenene.

Photocatalytic CO_2RR
In response to growing environmental concerns and energy scarcity, research on converting CO_2 to solar fuel through photoreduction has emerged. Similar to the photocatalytic water splitting, direct Z-scheme vdW heterostructures based on graphitic CN have been studied quite extensively, in addition to Bi-based heterostructures.
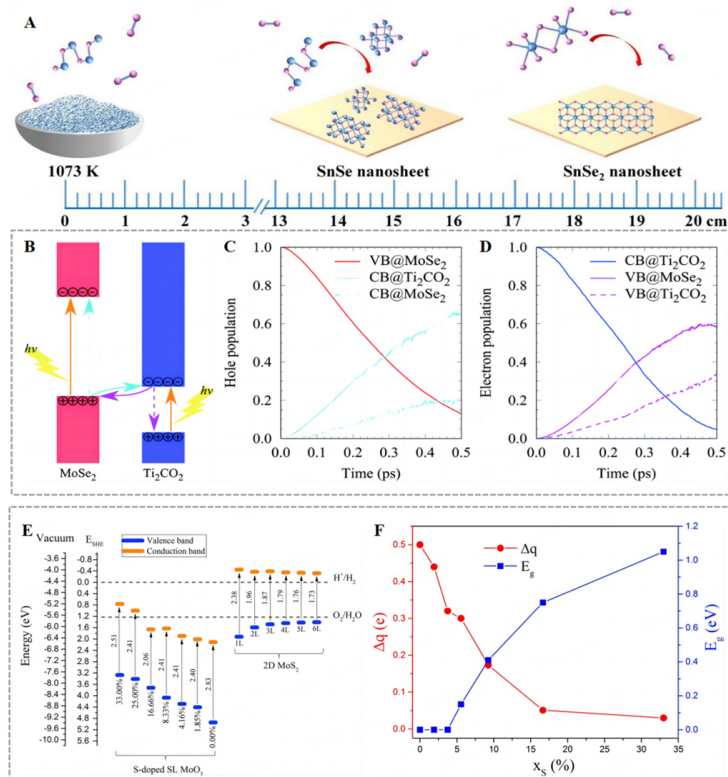
Figure 10. (A) Schematic diagram of the physical vapor deposition growth process, showing that SnSe nanosheets can be synthesized onto the ITO substrate with the source-substrate distance of 13-16 cm with the temperature of 860 K, and $SnSe_2$ nanosheets can be synthesized on the ITO substrate with the source-substrate distance of 17-20 cm with the temperature of 610 K. (Reproduced with permission[56]. Copyright 2023, American Chemical Society); (B) Schematic diagram of the photogenerated carrier transfer pathway for the $MoSe_2/Ti_2CO_2$ heterostructure. (Reproduced with permission[57]. Copyright 2021, Royal Society of Chemistry); (C and D) The time-dependent hole and electron population. (Reproduced with permission[57]. Copyright 2021, Royal Society of Chemistry); (E) Calculated conduction and valence band edge positions for S-substituted SL MoO_3 and 1-6L MoS_2 with respect to the vacuum level and the standard H_2 electrode. The lower edge of the conduction band (orange color) and the upper edge of the valence band (blue color) are presented along with the band gap in electron volts. The dashed black lines indicate the water stability limits for H_2 and oxygen evolution. The absolute potential of the standard H_2 electrode was taken as 4.44 eV at pH = 0. (Reproduced with permission[61]. Copyright 2021, American Chemical Society); (F) Evolution of the band gap and the Bader charge transfer (from MoS_2 layer to $MoO_{3-x}S_x$ layer) of the S-doped MoO_3/MoS_2 heterostructure as a function of the sulfur concentration in the MoO_3 layer. (Reproduced with permission[61]. Copyright 2021, American Chemical Society).

*Graphitic carbon nitride-based materials*

Fan *et al.* investigated a 2D C_2N/aza-CMP direct Z-scheme heterostructure consisting of an ultrathin aza-fused conjugated microporous polymer (aza-CMP) and C_2N[66]. Since the reduction potential of this heterostructure is not sufficient to drive CO_2RR, a Cu dimer is introduced to be anchored on the C_2N monolayer. The results show that the $Cu_2@C_2N$/aza-CMP heterostructure can significantly lower the reaction energy barrier, allowing CO_2RR to proceed spontaneously, and that the Cu-dimer is favorable for promoting the separation of photogenerated carriers at the interface of the heterostructure. Figure 12 illustrates the reaction pathways for CO_2RR and OER, with the generation of CH_4 being the most favorable from a thermodynamic point of view. The introduction of Cu-dimer improves the conversion rate of CO_2RR products and is beneficial for the generation of CH_4. This study is informative for the means of photocatalyst modification using metal atoms to lower the reaction energy barriers and for the modulation of specific reduction products.
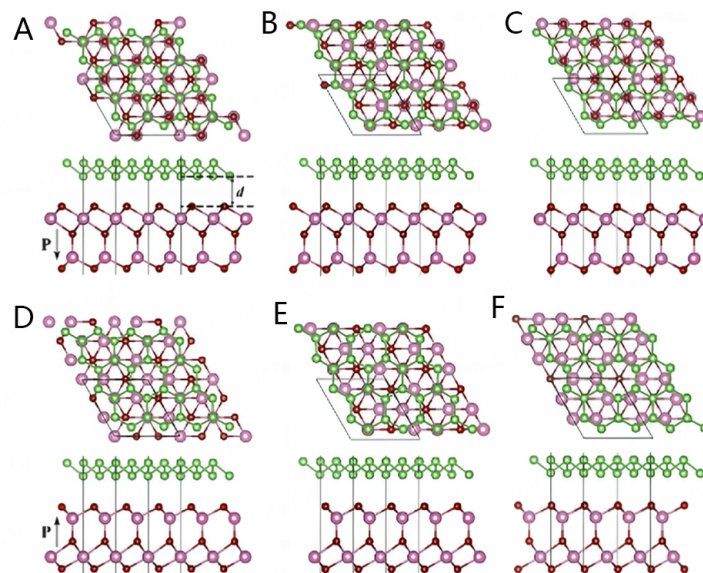
Figure 11. Two different stacking configurations are used in the construction of the α-In$_2$Se$_3$/arsenene vdW heterostructures because the α-In$_2$Se$_3$ layer has a different ferroelectric polarisation orientation, where A, B and C belong to Configuration I and D, E and F belong to Configuration II. The spontaneous out-of-plane electrode polarisation P in Configuration II points in the arsenene direction, whereas P in Configuration I points in the opposite direction. (Reproduced with permission[65]. Copyright 2022, Elsevier).

Based on the weak affinity and high activation energy for CO_2 of g-C$_3$N$_4$, Wang *et al.* introduced covalent organic frameworks (COFs) to modulate the photocatalytic CO_2RR performance of g-C$_3$N$_4$, mainly depending on the effective CO_2 adsorption and enhanced migration of photogenerated carriers through the off-domain of p-electrons supported by imide-conjugated COFs[67]. The performance of the g-C$_3$N$_4$/COF heterostructure is further improved by introducing N vacancies into g-C$_3$N$_4$. Photocatalytic performance test results show that the g-C$_3$N$_4$(NH)/COF heterostructure exhibits a high CO selectivity of 90.4%, with a high CO production rate of up to 11.25 µmol/h under visible light, which is 44 and 14 times higher than that of the pristine g-C$_3$N$_4$ and the heterostructure without N defects, respectively.

Aiming at the low solar-to-fuel energy conversion efficiency (SFE) in the photocatalytic CO_2RR process, Bian *et al.* proposed to improve SFE by introducing a wide band gap oxide semiconductor as an energy platform for the reduction photocatalyst to further enhance the separation of photogenerated carriers[68]. Specifically, a (001)TiO$_2$-g-C$_3$N$_4$/BiVO$_4$ (T-CN/BVNS) 2D heterostructure was constructed [Figure 13A], with the CBM of the heterostructure mainly contributed by g-C$_3$N$_4$ and the VBM mainly contributed by BiVO$_4$, while the (001)TiO$_2$ acts as an energy platform to converge electrons from the CB of g-C$_3$N$_4$ to its own CB, where the reduction reaction takes place. Consequently, the photocatalytic activity of the 5T-15CN/BVNS heterostructure was boosted greatly compared to 15CN/BVNS for both CO_2RR and pure water splitting [Figure 13B and C]. More importantly, this study provides a new guideline for developing advanced heterostructures based on narrow-band gap photocatalysts (e.g., WO$_3$, Fe$_2$O$_3$, *etc.*) by introducing wide band gap oxide semiconductors (e.g., SnO$_2$, *etc.*) as energy platforms. He *et al.* designed and fabricated zero-dimensional Ti$_3$C$_2$ quantum dots-decorated TiO$_2$/C$_3$N$_4$ (T-CN-TC) to precisely address the low utilization of photogenerated carriers for CO_2RR due to the slow reaction dynamics on the TiO$_2$/C$_3$N$_4$ (T-CN) heterostructure surfaces [Figure 13D-G][69]. Steady-state photoluminescence (PL) emission spectra show that the PL intensity of T-CN-TC is significantly lower than that of T-CN, implying that the intrinsic radiative recombination of photogenerated electron–hole pairs in T-CN-TC has been substantially inhibited by the introduced Ti$_3$C$_2$ quantum dots. This is due to the fact that Ti$_3$C$_2$ has a relatively lower Fermi level with respect to g-C$_3$N$_4$; thus, it can pool free electrons from the CBM of g-C$_3$N$_4$ to its own CBM for promoting photogenerated carrier separation. This can improve the utilization of photogenerated electrons in T-CN-TC, which is favorable for the photocatalytic performance. Moreover, Ti$_3$C$_2$ has a lower CO_2
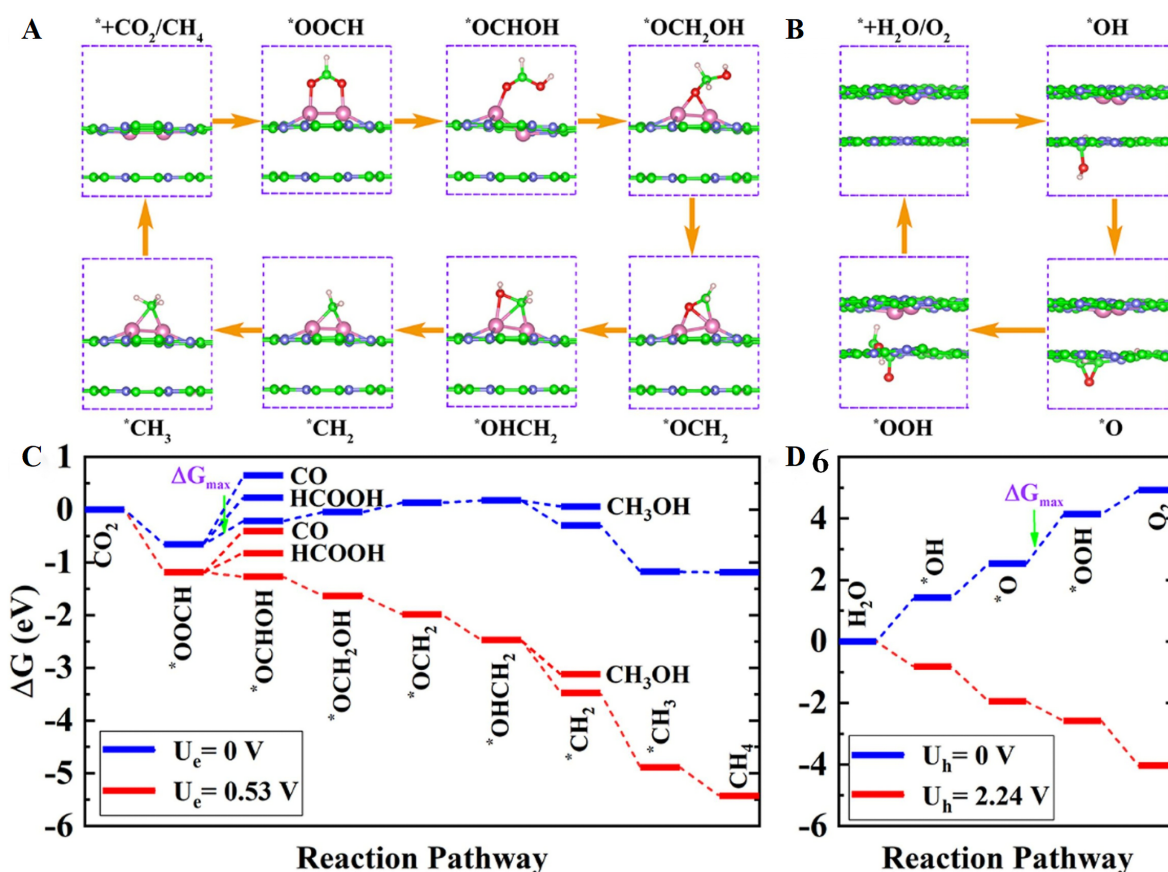
Figure 12. (A) CO_2RR and (B) OER photocatalytic pathways within C_2N/aza-CMP heterostructure. Red balls stand for O atoms, while the white balls indicate H atoms. (Reproduced with permission[66]. Copyright 2020, Elsevier); (C) The diagrams regarding free energy for the $8e^-$ pathways of CO_2RR within C_2N/aza-CMP heterostructure at diverse voltages. (Reproduced with permission[66]. Copyright 2020, Elsevier); (D) The diagrams regarding free energy for the $4e^-$ pathways of OER within C_2N/aza-CMP heterostructure at diverse voltages. The photogenerated holes and electrons provide the potentials of $U_h = 2.24$ V and $U_e = 0.53$ V, separately. (Reproduced with permission[66]. Copyright 2020, Elsevier).

activation energy and can provide more active sites. Photocatalytic CO_2RR tests show that T-CN-TC has the highest CO and CH_4 production rate with good stability, four and nine times higher than those of g-C_3N_4 and TiO_2, respectively [Figure 13F and G].

Bi-based materials

Beyond the widely used graphite carbon nitride-based materials, Bi-based materials have also been studied in the field of photocatalytic CO_2RR. Since BiOI has a strong reduction capacity and a narrow band gap suitable for visible-light photocatalysis, Wang *et al.* designed and fabricated a 2D Bi_2MoO_6/BiOI heterostructure in response to the high carrier conformality and excessive energy barrier of CO_2RR[70]. Thanks to the interleaved $[Bi_2O_2]^{2+}$ and MoO_4^{2-}/I^- ionic layers, both Bi_2MoO_6 and BiOI in Bi_2MoO_6/BiOI heterostructure possess spontaneous polarization and internal electric field, which are beneficial for accelerating the separation of photogenerated carriers. As shown in Figure 14, the heterostructure can effectively promote charge transfer due to the large interaction surface at the interfaces. What is more, the energy barrier of the heterostructure for photocatalytic CO_2RR was reduced by 0.35 eV compared with that
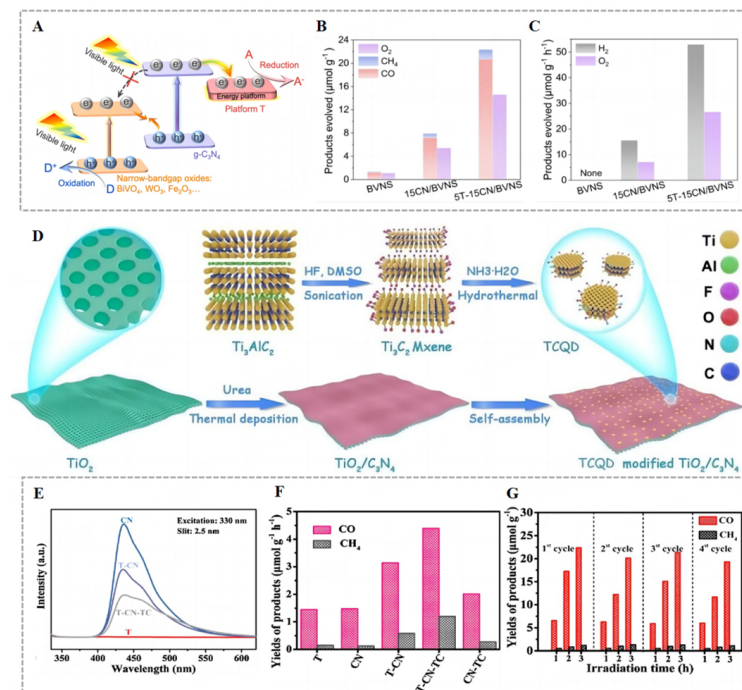
Figure 13. (A) Schematic representation of the proposed cascade Z-scheme mechanism of photogenerated charge transfer under visible light for efficient photocatalysis. T refers to (001)TiO_2, which can feasibly be replaced by other wide band gap semiconductors such as SnO_2. (Reproduced with permission[68]. Copyright 2021, Wiley-VCH); (B) Visible light irradiation for 4h of BVNS, 15CN/BVNS, and 5T-15CN/BVNS for CO_2RR. For yT-xCN/BVNS, x and y represent the mass percentage of CN and T to BVNS, respectively. (Reproduced with permission[68]. Copyright 2021, Wiley-VCH); (C) Visible light irradiation of BVNS, 15CN/BVNS, and 5T-15CN/BVNS for water splitting. The overall water splitting was carried out with Pt as the cocatalyst and without any sacrificial agents. (Reproduced with permission[68]. Copyright 2021, Wiley-VCH); (D) Schematic of the synthesis of ultrathin Ti_3C_2 quantum dots anchored TiO_2/C_3N_4 core-shell nanosheets. (Reproduced with permission[69]. Copyright 2020, Elsevier); (E) PL spectra of the samples of CN,T-CN and T-CN-TC. (Reproduced with permission[69]. Copyright 2020, Elsevier); (F) Photocatalytic CO_2 reduction performance of T, CN,T-CN, T-CN-TC and CN-TC after irradiation for 1h. (Reproduced with permission[69]. Copyright 2020, Elsevier); (G) The stability test of CO_2 reduction over T-CN-TC. (Reproduced with permission[69]. Copyright 2020, Elsevier).
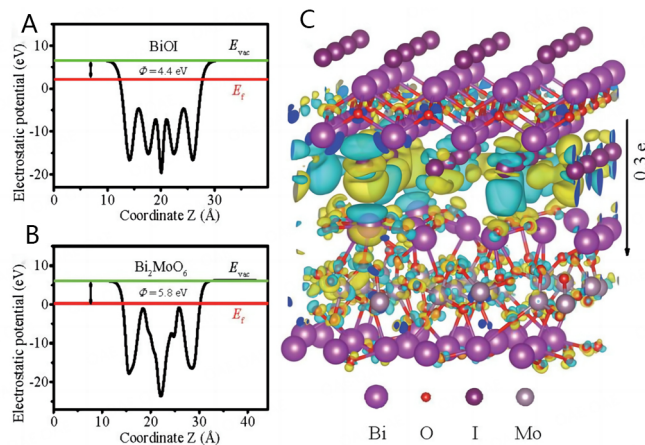
Figure 14. Work function profiles of (A) BiOI and (B) Bi_2MoO_6; (C) Charge density difference of Bi_2MoO_6/BiOI composite with an isosurface of 3×10^{-4} e/Å^3. (Reproduced with permission[70]. Copyright 2022, Elsevier).

of BiOI. In addition, this study found that the product generation rate was determined by CO_2 hydrogenation through density functional theory calculations[65]. Based on this study, it is expected to further develop direct Z-scheme vdW heterostructures constructed by Bi-based materials with other

materials, especially oxide semiconductors, to optimize the advantages of the low CBM position and narrow band gap of Bi-based materials.

CONCLUSIONS AND OUTLOOK

A direct Z-scheme vdW heterostructure is a promising photocatalytic system for solar–chemical energy conversion, which has some prominent advantages, mainly including effective separation of photogenerated carriers, strong redox driving force, simple construction, and minimized crystal defects. In the past decade, a variety of advanced direct Z-scheme vdW heterostructures have been developed for artificial photosynthesis. In this work, we briefly introduce the application of direct Z-scheme vdW heterostructures for photocatalytic water splitting and CO_2RR in the last five years. It is found that graphitic CN-based direct Z-scheme vdW heterostructures have exhibited excellent application fundamentals for both photocatalytic water splitting and CO_2RR. Meanwhile, heterostructures based on TMDs and arsenene are primarily utilized in water splitting applications, and Bi-based heterostructures exhibit promising potential for CO_2RR. Building on this, to enhance the photocatalytic efficiency of these heterostructures further, it is proposed that future research endeavors focus on the following key areas: (1) Heteroatoms doping plays a significant role in improving the energy band matching of the heterostructures and reducing the reaction energy barriers. In particular, to address the problems of the high energy barrier of CO_2RR, and as part of the vdW heterostructures do not meet the requirements of CO_2 reduction potential, doping metal atoms can be a good choice for reducing the reaction energy barrier, accelerating the interlayer recombination of invalid electrons and holes and strengthening the separation of the stronger redox-capable photogenerated carriers; (2) Applying appropriate tensile or compressive strains to the composite photocatalyst systems is effective in improving the absorption spectra of photocatalysts; (3) Utilizing the intrinsic dipoles of polar materials. For polar materials, if the orientation of the intrinsic dipole aligns with the built-in electric field within the heterostructure layers, this alignment can bolster the strength of the electric field. Such reinforcement leads to an increased potential drop between the constituent layers, thereby facilitating the separation and mobility of photogenerated carriers; (4) Surface passivation to reduce defects. Al_2O_3 can be introduced to passivate the defects on the heterostructure surface, thus effectively reducing the surface recombination of photogenerated charges focusing on the surface defects; (5) The insufficient CO_2 adsorption capacity can be improved by introducing COFs with high CO_2 adsorption capacity; (6) Considering the sluggish surface reaction kinetics inherent to CO_2RR, the lifetime of photogenerated electrons should be significantly extended. This is achievable by incorporating an energy platform within the heterostructure. This platform should possess a CBM potential that is more positive than the reduction photocatalyst yet more negative than the reduction potential of the CO_2RR. Such a strategy optimizes electron retention, facilitating more efficient reduction processes.

DECLARATIONS

Authors' contributions
Conceptualization and writing-original draft: Guan X, Hu K, Tian J
Writing-review and editing, supervision, and funding acquisition: Guan X, Zhao D, Zhou Z

Availability of data and materials
Not applicable.

Conflicts of interest

All authors declared that there are no conflicts of interest.

Ethical approval and consent to participate

Not applicable.

Consent for publication

Not applicable.

REFERENCES

1.   Energy Institute. Statistical Review of World Energy. 72nd ed. London: Energy Institute; 2023. p. 3.

2.   Acar C, Dincer I, Naterer GF. Review of photocatalytic water-splitting methods for sustainable hydrogen production. *Int J Energy Res* 2016;40:1449-73. DOI

3.   Fujishima A, Honda K. Electrochemical photolysis of water at a semiconductor electrode. *Nature* 1972;238:37-8. DOI

4.   Gao X, Dai C, Xu ZJ, Lawrence NS, Fisher AC. An electrochemical method for monitoring the acidity of water for fuel cell and environmental applications. *Energy Tech* 2018;6:94-9. DOI

5.   Mao M, Xu J, Li Y, Liu Z. Hydrogen evolution from photocatalytic water splitting by $LaMnO_3$ modified with amorphous CoS_x. *J Mater Sci* 2020;55:3521-37. DOI

6.   Liu L, Huang H, Chen F, et al. Cooperation of oxygen vacancies and 2D ultrathin structure promoting CO_2 photoreduction performance of $Bi_4Ti_3O_{12}$. *Sci Bull* 2020;65:934-43. DOI

7.   Moradi M, Khorasheh F, Larimi A. Pt nanoparticles decorated Bi-doped TiO_2 as an efficient photocatalyst for CO_2 photo-reduction into CH_4. *Solar Energy* 2020;211:100-10. DOI

8.   Tahir M, Tahir B. 2D/2D/2D $O-C_3N_4/Bt/Ti_3C_2T_x$ heterojunction with novel MXene/clay multi-electron mediator for stimulating photo-induced CO_2 reforming to CO and CH_4. *Chem Eng J* 2020;400:125868. DOI

9.   Jiang Z, Ye Z, Shangguan W. Recent advances of hydrogen production through particulate semiconductor photocatalytic overall water splitting. *Front Energy* 2022;16:49-63. DOI

10.   Chen M, Sun T, Zhao W, et al. In situ growth of metallic $1T-MoS_2$ on TiO_2 nanotubes with improved photocatalytic performance. *ACS Omega* 2021;6:12787-93. DOI

11.   Li Y, Sadaf SM, Zhou B. Ga(X)N/Si nanoarchitecture: An emerging semiconductor platform for sunlight-powered water splitting toward hydrogen. *Front Energy* 2024;18:56-79. DOI

12.   Wang Z, Li C, Domen K. Recent developments in heterogeneous photocatalysts for solar-driven overall water splitting. *Chem Soc Rev* 2019;48:2109-25. DOI

13.   Li H, Du H, Luo H, Wang H, Zhu W, Zhou Y. Recent developments in metal nanocluster-based catalysts for improving photocatalytic CO_2 reduction performance. *Microstructures* 2023;3:2023024. DOI

14.   Wang J, Wang S. A critical review on graphitic carbon nitride $(g-C_3N_4)$-based materials: preparation, modification and environmental application. *Coordin Chem Rev* 2022;453:214338. DOI

15.   Wang J, Sun S, Zhou R, et al. A review: synthesis, modification and photocatalytic applications of $ZnIn_2S_4$. *J Mater Sci Technol* 2021;78:1-19. DOI

16.   Yi J, El-alami W, Song Y, Li H, Ajayan PM, Xu H. Emerging surface strategies on graphitic carbon nitride for solar driven water splitting. *Chem Eng J* 2020;382:122812. DOI

17.   Luo B, Zhao Y, Jing D. State-of-the-art progress in overall water splitting of carbon nitride based photocatalysts. *Front Energy* 2021;15:600-20. DOI

18.   Zhao D, Guan X, Shen S. Design of polymeric carbon nitride-based heterojunctions for photocatalytic water splitting: a review. *Environ Chem Lett* 2022;20:3505-23. DOI

19.   Chen M, Chang W, Zhang J, Zhao W, Chen Z. Preparation of a hybrid TiO_2 and $1T/2H-MoS_2$ photocatalyst for the degradation of tetracycline hydrochloride. *ACS Omega* 2023;8:15458-66. DOI

20.   Low J, Jiang C, Cheng B, Wageh S, Al-ghamdi AA, Yu J. A review of direct Z-scheme photocatalysts. *Small Methods* 2017;1:1700080. DOI

21.   Das S, Deka T, Ningthoukhangjam P, Chowdhury A, Nair RG. A critical review on prospects and challenges of metal-oxide embedded $g-C_3N_4$-based direct Z-scheme photocatalysts for water splitting and environmental remediation. *Appl Surf Sci Adv* 2022;11:100273. DOI

22.   Belessiotis GV, Kontos AG. Plasmonic silver (Ag)-based photocatalysts for H_2 production and CO_2 conversion: review, analysis and perspectives. *Renew En* 2022;195:497-515. DOI

23. Bard AJ. Photoelectrochemistry and heterogeneous photo-catalysis at semiconductors. *J Photoch* 1979;10:59-75. DOI

24. Wang X, Liu G, Chen ZG, et al. Enhanced photocatalytic hydrogen evolution by prolonging the lifetime of carriers in ZnO/CdS heterostructures. *Chem Commun* 2009;23:3452-4. DOI

25. Xu Q, Zhang L, Yu J, Wageh S, Al-ghamdi AA, Jaroniec M. Direct Z-scheme photocatalysts: principles, synthesis, and applications. *Mater Today* 2018;21:1042-63. DOI

26. Fu J, Xu Q, Low J, Jiang C, Yu J. Ultrathin 2D/2D WO_3/g-C_3N_4 step-scheme H_2-production photocatalyst. *Appl Catal B Environ* 2019;243:556-65. DOI

27. Chen W, Liu T, Huang T, et al. A novel yet simple strategy to fabricate visible light responsive C,N-TiO_2/g-C_3N_4 heterostructures with significantly enhanced photocatalytic hydrogen generation. *RSC Adv* 2015;5:101214-20. DOI

28. Low J, Dai B, Tong T, Jiang C, Yu J. In situ irradiated X-ray photoelectron spectroscopy investigation on a direct Z-scheme TiO_2 /CdS composite film photocatalyst. *Adv Mater* 2019;31:e1807920. DOI

29. Koma A, Sunouchi K, Miyajima T. Fabrication and characterization of heterostructures with subnanometer thickness. *Microelectron Eng* 1984;2:129-36. DOI

30. Lou P, Lee JY. GeC/GaN vdW heterojunctions: a promising photocatalyst for overall water splitting and solar energy conversion. *ACS Appl Mater Interfaces* 2020;12:14289-97. DOI PubMed

31. Xu Y, Jin X, Ge T, et al. Realizing efficient CO_2 photoreduction in Bi_3O_4Cl: constructing van der Waals heterostructure with g-C_3N_4. *Chem Eng J* 2021;409:128178. DOI

32. Rahimi K, Moshfegh AZ. Band alignment tuning of heptazine-g-C_3N_4/g-ZnO vdW heterostructure as a promising water-splitting photocatalyst. *Phys Chem Chem Phys* 2021;23:20675-85. DOI

33. Wenna H, Xuefeng C, Minglei J, et al. A direct Z-scheme g-C_6N_6/InP van der Waals heterostructure: a promising photocatalyst for high-efficiency overall water splitting. *J Phys D: Appl Phys* 2022;55:264001. DOI

34. Zhang Y, Qiao H, Yan Z, Duan L, Ni L, Fan J. PtS_2/g-C_3N_4 van der Waals heterostructure: a direct Z-scheme photocatalyst with high optical absorption, solar-to-hydrogen efficiency and catalytic activity. *Int J Hydrogen* 2023;48:14659-69. DOI

35. Yang J, Wei X, Wang Z, et al. The direct Z-scheme g-C_6N_6/WTe_2 van der Waals heterojunction as photocatalyst over water splitting in the visible light: designing strategy from first principles. *J Photoch Photobio A* 2023;435:114263. DOI

36. Zhang R, Zhang L, Zheng Q, Gao P, Zhao J, Yang J. Direct Z-scheme water splitting photocatalyst based on two-dimensional van der waals heterostructures. *J Phys Chem Lett* 2018;9:5419-24. DOI

37. Wang J, Zhang X, Song X, Fan Y, Zhang Z, Zhao M. Insights into photoinduced carrier dynamics and overall water splitting of Z-scheme van der waals heterostructures with intrinsic electric polarization. *J Phys Chem Lett* 2023;14:798-808. DOI

38. Wang Z, Luo Z, Li J, Yang K, Zhou G. 2D van der Waals heterostructures of graphitic BCN as direct Z-scheme photocatalysts for overall water splitting: the role of polar π-conjugated moieties. *Phys Chem Chem Phys* 2020;22:23735-42. DOI

39. Dong H, Hong S, Zhang P, et al. Metal-free Z-scheme 2D/2D VdW heterojunction for high-efficiency and durable photocatalytic H_2 production. *Chem Eng J* 2020;395:125150. DOI

40. Meng J, Wang J, Wang J, Li Q, Yang J. C_7N_6/Sc_2CCl_2 weak van der waals heterostructure: a promising visible-light-driven Z-scheme water splitting photocatalyst with interface ultrafast carrier recombination. *J Phys Chem Lett* 2022;13:1473-9. DOI

41. Wang B, Wang X, Wang P, et al. Bilayer $MoSe_2$/HfS_2 nanocomposite as a potential visible-light-driven Z-scheme photocatalyst. *Nanomaterials* 2019;9:1706. DOI PubMed PMC

42. Zheng X, Yang L, Li Y, Yang L, Luo S. Direct Z-scheme $MoSe_2$ decorating TiO_2 nanotube arrays photocatalyst for water decontamination. *Electrochim Acta* 2019;298:663-9. DOI

43. Meng A, Zhu B, Zhong B, Zhang L, Cheng B. Direct Z-scheme TiO_2/CdS hierarchical photocatalyst for enhanced photocatalytic H_2-production activity. *Appl Surf Sci* 2017;422:518-27. DOI

44. Ren K, Tang W, Sun M, Cai Y, Cheng Y, Zhang G. A direct Z-scheme PtS_2/arsenene van der Waals heterostructure with high photocatalytic water splitting efficiency. *Nanoscale* 2020;12:17281-9. DOI

45. Zhang Q, Ren K, Zheng R, Huang Z, An Z, Cui Z. First-principles calculations of two-dimensional CdO/HfS_2 van der Waals heterostructure: direct Z-scheme photocatalytic water splitting. *Front Chem* 2022;10:879402. DOI PubMed PMC

46. Li H, Xu L, Huang X, et al. Two-dimensional C_3N/WS_2 vdW heterojunction for direct Z-scheme photocatalytic overall water splitting. *Int J Hydrogen* 2023;48:2186-99. DOI

47. Singh A, Jain M, Bhattacharya S. MoS_2 and Janus (MoSSe) based 2D van der Waals heterostructures: emerging direct Z-scheme photocatalysts. *Nanoscale Adv* 2021;3:2837-45. DOI PubMed PMC

48. Wang B, Wang X, Wang P, et al. Bilayer $MoTe_2$/XS_2 (X = Hf, Sn, Zr) heterostructures with efficient carrier separation and light absorption for photocatalytic water splitting into hydrogen. *Appl Surf Sci* 2021;544:148842. DOI

49. Cao M, Ni L, Wang Z, et al. DFT investigation on direct Z-scheme photocatalyst for overall water splitting: $MoTe_2$/BAs van der Waals heterostructure. *Appl Surf Sci* 2021;551:149364. DOI

50. Zhu XT, Xu Y, Cao Y, Zou DF, Sheng W. Direct Z-scheme arsenene/HfS_2 van der Waals heterojunction for overall photocatalytic water splitting: first-principles study. *Appl Surf Sci* 2022;574:151650. DOI

51. Luo Q, Yin S, Sun X, Tang Y, Feng Z, Dai X. GaN/BS van der Waals heterostructure: a direct Z-scheme photocatalyst for overall water splitting. *Appl Surf Sci* 2023;609:155400. DOI

52. Liu J, Shen Y, Lv L, et al. Rational design direct Z-scheme β-GeSe/HfS_2 heterostructure by interfacial engineering: efficient photocatalyst for overall water splitting in the wide solar spectrum. *Appl Surf Sci* 2022;589:153025. DOI

53.   Cao J, Zhang X, Zhao S, Wang S, Cui J. Mechanism of photocatalytic water splitting of 2D WSeTe/XS$_2$ (X = Hf, Sn, Zr) van der Waals heterojunctions under the interaction of vertical intrinsic electric and built-in electric field. *Appl Surf Sci* 2022;599:154012. DOI

54.   Zhang Y, Shen Y, Liu J, et al. Internal electric field enhanced photoelectrochemical water splitting in direct Z-scheme GeC/HfS$_2$ heterostructure: a first-principles study. *Appl Phys Lett* 2023;122:043902. DOI

55.   Christopher ES, Yury G. MXenes: a tunable family of 2D carbides and nitrides. Available from: https://www.sigmaaldrich.com/US/en/technical-documents/technical-article/materials-science-and-engineering/organic-electronics/mxenes [Last accessed on 7 Apr 2024].

56.   Lu C, Dong W, Zou Y, et al. Direct Z-scheme SnSe$_2$/SnSe heterostructure passivated by Al$_2$O$_3$ for highly stable and sensitive photoelectrochemical photodetectors. *ACS Appl Mater Interfaces* 2023;15:6156-68. DOI

57.   Fu CF, Li X, Yang J. A rationally designed two-dimensional MoSe$_2$/Ti$_2$CO$_2$ heterojunction for photocatalytic overall water splitting: simultaneously suppressing electron-hole recombination and photocorrosion. *Chem Sci* 2021;12:2863-9. DOI PubMed PMC

58.   Liu X, Cheng P, Zhang X, et al. Enhanced solar-to-hydrogen efficiency for photocatalytic water splitting based on a polarized heterostructure: the role of intrinsic dipoles in heterostructures. *J Mater Chem A* 2021;9:14515-23. DOI

59.   Ju L, Tang X, Kou L. Polarization boosted catalysis: progress and outlook. *Microstructures* 2022;2:2022008. DOI

60.   Jalil A, Zhao T, Kanwal A, Ahmed I. Prediction of direct Z-scheme H and H-phase of MoSi$_2$N$_4$/MoSX (X = S, Se) van der Waals heterostructures: a promising candidate for photocatalysis. *Chem Eng J* 2023;470:144239. DOI

61.   Shahrokhi M, Raybaud P, Le Bahers T. 2D MoO$_{3-x}$S$_x$/MoS$_2$ van der Waals assembly: a tunable heterojunction with attractive properties for photocatalysis. *ACS Appl Mater Interfaces* 2021;13:36465-74. DOI

62.   Zeng H, Zhao J, Cheng AQ, Zhang L, He Z, Chen RS. Tuning electronic and optical properties of arsenene/C$_3$N van der Waals heterostructure by vertical strain and external electric field. *Nanotechnology* 2018;29:075201. DOI

63.   Zhang S, Yan Z, Li Y, Chen Z, Zeng H. Atomically thin arsenene and antimonene: semimetal-semiconductor and indirect-direct band-gap transitions. *Angewandte Chemie* 2015;127:3155-8. DOI

64.   Kamal C, Ezawa M. Arsenene: two-dimensional buckled and puckered honeycomb arsenic systems. *Phys Rev B* 2015;91:085423. DOI

65.   Lu Q, Zhang L, Xu T, Zhang B, Gong W. Highly efficient photocatalytic water splitting in direct Z-scheme α -In$_2$Se$_3$/are van der Waals heterostructures. *Surfaces Interfaces* 2023;36:102608. DOI

66.   Fan Y, Qi S, Li W, Zhao M. Direct Z-scheme photocatalytic CO$_2$ conversion to solar fuels in a two-dimensional C$_2$N/aza-CMP heterostructure. *Appl Surf Sci* 2021;541:148630. DOI

67.   Wang J, Yu Y, Cui J, et al. Defective g-C$_3$N$_4$/covalent organic framework van der Waals heterojunction toward highly efficient S-scheme CO$_2$ photoreduction. *Appl Catal B Environ* 2022;301:120814. DOI

68.   Bian J, Zhang Z, Feng J, et al. Energy platform for directed charge transfer in the cascade Z-scheme heterojunction: CO$_2$ photoreduction without a cocatalyst. *Angew Chem Int Ed* 2021;60:20906-14. DOI PubMed PMC

69.   He F, Zhu B, Cheng B, Yu J, Ho W, Macyk W. 2D/2D/0D TiO$_2$/C$_3$N$_4$/Ti$_3$C$_2$ MXene composite S-scheme photocatalyst with enhanced CO$_2$ reduction activity. *Appl Catal B Environ* 2020;272:119006. DOI

70.   Wang Z, Cheng B, Zhang L, et al. S-Scheme 2D/2D Bi$_2$MoO$_6$/BiOI van der Waals heterojunction for CO$_2$ photoreduction. *Chinese J Catal* 2022;43:1657-66. DOI